Electron beam lithography of GeTe through polymorphic phase transformation

Hu Zhang
State Key Laboratory for Mechanical Behavior of Materials
Meng Li
Queensland University of Technology
Shao-Dong Cheng
The School of Electronic and Information Engineering
Lu Lu
Ji Hua Laboratory
Zhi-Gang Chen
Queensland University of Technology https://orcid.org/0000-0002-9309-7993
Hengqiang Ye
Institute of Metals Research
Shao-Bo Mi (mi_jhlab@163.com)
Ji Hua Laboratory https://orcid.org/0000-0001-5711-850X

Article

Keywords:

Posted Date: June 9th, 2023

DOI: https://doi.org/10.21203/rs.3.rs-3004049/v1

Additional Declarations: There is **NO** Competing Interest.

Electron beam lithography of GeTe through polymorphic phase transformation

Hu Zhang[1,2,5] Meng Li[3.5], Shao-Bo Mi[1,4], Shao-Dong Cheng[2], Lu Lu[1], Zhi-Gang Chen[3], Heng-Qiang Ye[1]

[1]*Ji Hua Laboratory, Foshan 528200, China*

[2]*State Key Laboratory for Mechanical Behavior of Materials, Xi'an Jiaotong University, Xi'an 710049, China*

[3]*School of Chemistry & Physics, Faculty of Science, Queensland University of Technology, Queensland 4000, Australia*

[4]*Foshan University, Foshan 528225, China*

[5]*These authors contributed equally: Hu Zhang, Meng Li.*

Corresponding authors:

Shao-Bo Mi, Email: mi_jhlab@163.com

Zhi-Gang Chen, Email: zhigang.chen@qut.edu.au

ABSTRACT

Finding new phases can deeply understand the fundamental of materials and broaden their practical applications. Here, we report two undiscovered phases of GeTe including the zinc-blende (c-) phase and the hexagonal (h-) phase with interlayer van der Waals gaps. A polymorphic phase transformation from rhombohedral α-GeTe to c- and h-GeTe near room temperature, then supposedly to cubic β-GeTe at higher temperature, is first realized via electron beam irradiation. Their underlying thermodynamics and kinetics are illustrated by the *in-situ* heating experiments and molecular dynamics simulation. Density-functional theory calculation indicates that c-GeTe exhibits typical metallic behavior and h-GeTe is a narrow-gap semiconductor with a strong spin-orbital coupling effect. An atomic-scale electron beam lithography technique is finally developed and adopted to fabricate GeTe-based quantum devices compromising nanopillars and heterostructures of c- and h-GeTe in α-GeTe matrix.

As a historic member of group IV–VI chalcogenides, germanium telluride (GeTe) was first known for its non-volatile ovonic memory switching behavior, which can be applied for high-speed, high-density, and multi-value memory technologies.[1, 2, 3] More recently, investigations on GeTe and its derivative antimonides and bismuthides have resurged, with heightened interest surrounding their intriguing phase-change crystallography,[4] nature of chemical bonds, [5] and underlying physical and chemical fundamentals.[6] Particularly, such a family of materials exhibits desirable electronic and thermal transport characteristics for thermoelectricity,[7, 8, 9] ferroelectricity,[10, 11, 12] information storage,[13] superconductivity.[14] These functionalities are based mainly on the entanglement or decoupling between the amorphous and crystalline phases of GeTe, thus being sensitive to the corresponding phase transformation.

Pristine GeTe alone undergoes a ferroelectric-like, reversible, and quasi-second ordered phase transformation from low-temperature rhombohedral α-GeTe ($R3m$) to high-temperature face-centered cubic β-GeTe ($Fm\bar{3}m$) at the Curie temperature (T_c) of ~720 K.[15] Specifically, in β-GeTe, the central Ge atom is six-fold coordinated with neighboring Te atoms, resulting in an O_h chemical bond scheme.[16] During the phase transformation, the O_h coordination symmetry switches to C_{3v} through splitting the six equivalent Ge–Te bonds into three long metavalent bonds and three short dative bonds.[17] Meanwhile, the rocksalt-type lattice of β-GeTe randomly shears along the four Peierls distortion vector, i.e., [111], [$\bar{1}$11], [1$\bar{1}$1], and [$\bar{1}\bar{1}$1], resulting in simultaneous polarization of Ge and Te sublattices.[18] The phase-change-induced evolutionary crystal structure and bonding mechanism lead to exceptional optical absorption and dielectric constant, and unconventionally large Born effective charge, making GeTe competent diverse functionalities.[19] Discovering additional phases is therefore crucial for broadening the application scope of GeTe-based functional materials. In fact, there have been previous reports of orthorhombic γ-GeTe (*Pnma*),[20] orthorhombic δ-GeTe (*Pbcn*),[21] and monoclinic ε-GeTe (*Cm*),[22] which are achieved either with non-stoichiometry or under ultrahigh isometric pressure, being

exempt from scalable synthesis and practical application. As a result, exploring easily achievable new phases of GeTe is still an open challenge in this field.

In this work, we report two room-temperature-stable phases of GeTe that have never been observed, namely zinc-blende c-GeTe and hexagonal h-GeTe with interlayer van der Waals gaps. Specifically, we first tailor the polymorphic phase transformation from α-GeTe to c-GeTe and h-GeTe via electron beam irradiation, which supposedly ends in β-GeTe at above the T_c. The thermodynamic and kinetic features behind this phenomenon are theoretically explained due to the stereochemical expression of Ge_4s^2 lone pairs and experimentally verified based on *in-situ* heating experiments. We further perform density-functional theory (DFT) calculation to understand the electronic transport characteristics of inclusive phases on the fundamental level. Last but foremost, two proof-of-concept GeTe-based quantum devices are successfully fabricated through patterning nanopillar arrays and heterostructures of h-GeTe and c-GeTe superlattices in α-GeTe matrix using electron beam lithography, which can significantly broaden the application scope of GeTe and other group IV–VI chalcogenides.

Results

Formation of c-GeTe and h-GeTe

We used SEM and XRD to identify the microstructures and phase purities of as-prepared samples. Fig. 1a displays an SE-SEM image of the fractured cross-section, which exhibits a typical herringbone structure with periodic twinning motifs. The alternative contrast between adjacent twinned domains should be attributed to the different variants of ferroelectric polarization when cooling from β-GeTe to α-GeTe. Fig. 1b shows an XRD pattern of the as-prepared GeTe sample at room temperature, where the majority of diffraction peaks can be indexed as α-GeTe. A minor Ge impurity phase (< 5 wt.%) arising from spinodal decomposition in binary Ge–Te phase diagram is also trackable, indicating the major GeTe phase is Ge-deficient. The lattice parameters of α-GeTe are calculated as a = 4.170(1) Å and c = 10.672(9) Å, being consistence with previous literatures.[23, 24, 25] To simplify the discussion, for

the time being, we consider α-GeTe as the pseudo-cubic analogy of β-GeTe with a lattice parameter of a = 5.900 Å, and mark relevant planes and axes with subscripted "pc". The bright-field (BF-TEM) image of GeTe in Fig. 1c displays contrast variation periodically owing to the twinned domains stacking in α-GeTe.[26, 27] The inset of SAED pattern further clarifies the crystallographic orientation in a single domain in the $[1\bar{1}0]_{pc}$ zone axis. Fig. 1d shows an atomic-resolution HAADF-STEM image of GeTe in the identical zone axis, indicating the off-centering displacement of Ge from the high-symmetry ground state along the $[111]_{pc}$ direction. The corresponding superposed structural model on the simulated HAADF-STEM image is provided in the inset for visualization.

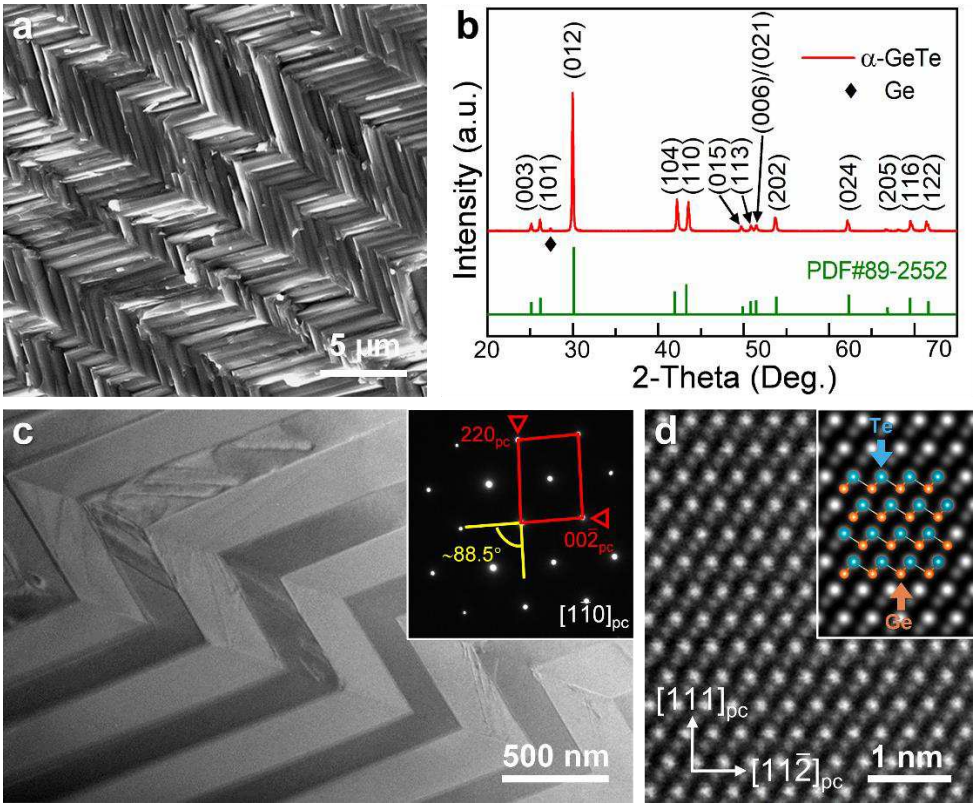

FIG. 1 Characterization of pristine α-GeTe. (a) Low-magnification SE-SEM image of fractography. (b) Experimental and reference XRD patterns at room temperature. (c) Low-magnification BF-TEM image, with the inset being the SAED pattern. (d) Atomic-resolution HAADF-STEM image, with the inset being superposed structure model on simulated HAADF-STEM image. The micrographs in (c–d) are in the $[1\bar{1}0]_{pc}$ zone axis.

Polymorphic phase transformation

As both XRD and SEM results suggested there are numerous Ge vacancies in GeTe samples, we examined the feasibility to modify these vacancies via electron beam irradiation. In fact, it has been previously reported modulating Ge vacancies in α-GeTe via nanosecond pulsed laser radiation to alter the multilevel reversible electrical conductivity of GeTe thin films.[28, 29] Other notable reports are about tunning the disorder degree of Ge vacancies in $Ge_2Sb_2Te_5$ via electron beam irradiation,[30, 31, 32] which leads to unique optical, electrical, and thermal properties.[33] In our experiment, we vary the time of electron beam irradiation on the region of interest (ROI) and take corresponding atomic-resolution HAADF- and ABF-STEM images in the $[1\bar{1}0]_{pc}$ zone axis. Under the HAADF-STEM mode, the intensity of atomic column is roughly proportional to squared atomic number (Z^2),[34] based on which the Te sublattices can be clearly distinguished. In contrast, under the ABF-STEM mode, the intensity is roughly proportional to $Z^{1/3}$,[35] which is often used to observe the lighter Ge sublattices. As shown in Fig. 2a–b, the 5×5 nm^2 ROI in the center of α-GeTe matrix becomes unstable when the probe current of electron beam is above 6.4 pA/cm^2, corresponding to a beam intensity of 1.6×10^{26} $e\cdot m^{-2}\cdot s^{-1}$. After 240 s of continuous electron beam irradiation, the Ge sublattices in ROI are drifted along the $[111]_{pc}$ direction, while the Te sublattices are arguably unaffected, leading to the formation of an unreported face-centered cubic phase of GeTe (see Movie S1), here named as c-GeTe.

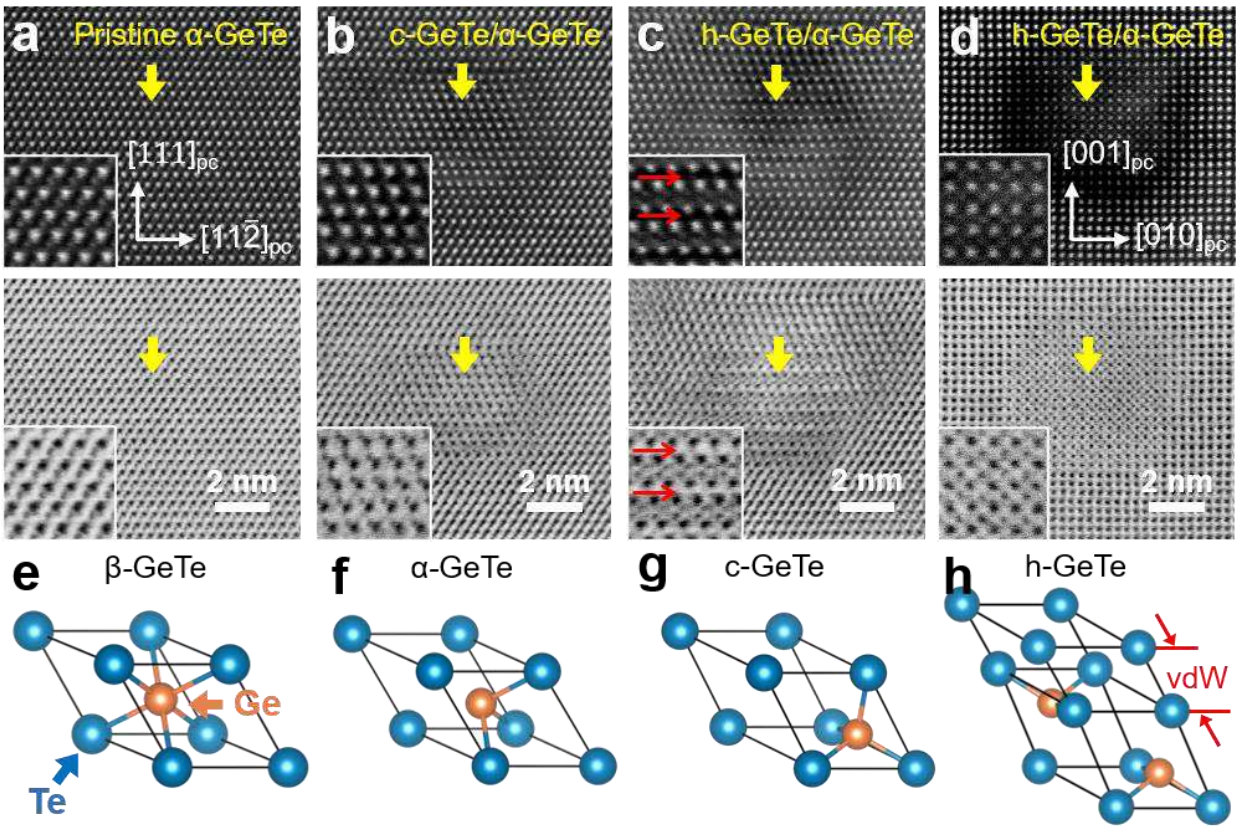

FIG. 2 HAADF- (upper) and ABF-STEM (down) images indicating the polymorphic phase transformation driven by electron beam irradiation. (a) Pristine α-GeTe. (b) ROI in α-GeTe after 240 s electron beam irradiation. (c) ROI in α-GeTe after 500 s electron beam irradiation. The micrographs in (a–c) are in the $[1\bar{1}0]_{pc}$ zone axis. (d) ROI in α-GeTe after 500 s electron beam irradiation in the $[100]_{pc}$ zone axis. The insets of (a–d) refer to magnified areas marked by yellow arrows. Note that vdW gaps can be observed in the $[1\bar{1}0]_{pc}$ zone axis while becoming invisible in the $[100]_{pc}$ zone axis, as marked by red arrows in the insets of (c). Structural models of different phases of GeTe are drawn for visualization. (e–f) Primitive cell of β-GeTe, α-GeTe, and c-GeTe, respectively. (h) Unit cell of h-GeTe.

By extending the electron beam irradiation to 500 s, further re-arrangement of Ge sublattices can happen, while Te sublattices, as one would expect, remain almost the same (see Fig. 2c). This leads to another unreported layered hexagonal phase of GeTe, here named as h-GeTe. Unlike the –Te–Ge– stacking sequence along the $[111]_{pc}$ direction in α-GeTe, the –Te–Ge–Ge–Te– stacking sequence is

allowed in h-GeTe due to simultaneous convergence of two adjacent Ge layers and divergence of two adjacent Te layers. Van der Waals (vdW) gaps exist between adjacent quadruple atomic layers.[36] It is worth mentioning that h-GeTe seems to be the stable phase under such an electron beam intensity, because no more crystalline phase can be observed even when extending the electron beam irradiation to about 2000 s. Supplementary HAADF- and ABF-STEM images of ROI in the $[100]_{pc}$ zone axis are presented in Fig. 2d. As can be seen, while the Ge and Te atomic columns of α-GeTe are overlapped when viewed in such a zone axis, they can be distinguished in c-GeTe and h-GeTe phases (See Fig. S1), where the Ge atomic column lies among four neighboring Te atomic columns.

The preceding micrographs suggest both c-GeTe and h-GeTe belong to distinct coordination symmetries and space groups compared with those of α-GeTe and β-GeTe (Fig. 2e–f), which lacks an inversion center. According to Fig. 2a–b, the evolution from α-GeTe to c-GeTe originates from the displacement of the central Ge atom in $GeTe_6$ octahedron along the $[111]_{pc}$ direction, which is ultimately in the interstitial of $GeTe_4$ tetrahedron. The c-GeTe is therefore identified as the zinc-blende structure ($F\bar{4}3m$, Fig. 2g).[31] According to Fig. 2b–d, the evolution from c-GeTe to h-GeTe can be regarded as one Ge atom hopping from the interstitial of $GeTe_4$ tetrahedron to the center of the adjacent vacant Te_4 tetrahedron. Meanwhile, the as-formed two consecutive Te_4 tetrahedra form the vdW gaps between two Te atomic layers. The h-GeTe is therefore identified as the hexagonal structure with an inversion center ($R\bar{3}m$, Fig. 2h), which has an OR of h-GeTe$(0001)[11\bar{2}0]$//α-GeTe$(111)_{pc}[1\bar{1}0]_{pc}$ relative to the α-GeTe matrix. Note that c-GeTe and h-GeTe may co-exist in a single ROI, as shown in Fig. S2 and Movie S1.

Thermodynamic and kinetic features

The thermodynamic and kinetic features of such a polymorphic phase transformation are complicated because the elastic and inelastic interaction between incident electrons and lamella TEM specimen may respectively trigger knock-on damage and radiolysis (breaking of chemical bonds). In the latter scenario, the driven force of phase transformation is proportional to the increase of specimen

temperature (ΔT) due to the inelastic scattering process, which can be calculated based on $\Delta T = (I\Delta E/\pi\kappa ed)\cdot\ln(b/r_0)$, where I, κ, e, ΔE, d, b, and r_0 are beam current, thermal conductivity, elementary charge, total energy loss, thickness and radius of interactive volume, and beam radius, respectively.[37] We here assume κ as 8.3 $W\cdot m^{-1}\cdot K^{-1}$ and $\Delta E/d$ as 0.97 $eV\cdot nm^{-1}$ according to literatures,[38, 39] and neglect their change in different phases. We also estimate I, b, and r_0 are 6.4 pA, 1.5 mm, and 0.07 nm, respectively, drawing to the value of ΔT as ~0.004 K, which implies that the radiolysis can hardly drive the phase transformation.

Coming to the elastic scattering process, the minimum energy of incident electrons ($E_0^{\min}$) to force an atomic displacement can be calculated based on $E_0^{\min} = (511\text{ keV})\cdot\left\{[1+AE_d/(561\text{ eV})]^{1/2}-1\right\}$, where A is atomic mass, and E_d is the displacement threshold energy (6.43 eV for Ge, and 7.90 eV for Te).[40, 41, 42] This results in the $E_0^{\min}$ of 180.8 keV for Ge and of 343.6 keV for Te, implying the knock-on effect is the primary driven force. The lower $E_0^{\min}$ of Ge than the accelerating voltage of the electron beam (200 keV) may explain the dynamic motion of Ge sublattices during the phase transformation. In contrast, the much higher $E_0^{\min}$ of Te than 200 keV means the Te sublattices are hardly drifted by electron beam, being more stable during the phase transformation.

To experimentally verify our viewpoint, we conduct the *in-situ* heating experiment with a temperature profile given in Fig. S3. It can be known from the HAADF- and ABF-STEM images in Fig. 3a that, with incrementing temperature, the c-GeTe in ROI is thermally stable until 475 K, which descends to α-GeTe when above 485 K. Such an Arrhenius barrier of ~200 K is posed to compensate for the knock-on effect due to 200 s electron beam irradiation, as illustrated in Fig. 3b. DFT calculation is performed to explain the polymorphic phase transformation from an energetic perspective. Since both c-GeTe and h-GeTe are coherently embedded in the α-GeTe matrix, their lattice parameters at room temperature are determined to be a = 5.900 Å for c-GeTe, and a = 4.172 Å and c = 20.438 Å for h-GeTe. We determine the linear thermal expansion parameters based on MD simulation, which are 1.8×10^{-5} K^{-1}, 7.1×10^{-6} K^{-1}, 9.8×10^{-6} K^{-1}, and 3.4×10^{-5} K^{-1} for α-GeTe, c-GeTe, h-GeTe, and β-GeTe,

respectively. The calculated temperature-dependent energies per atom are plotted in Fig. 3c, being consistent with Fig. 3a–b.

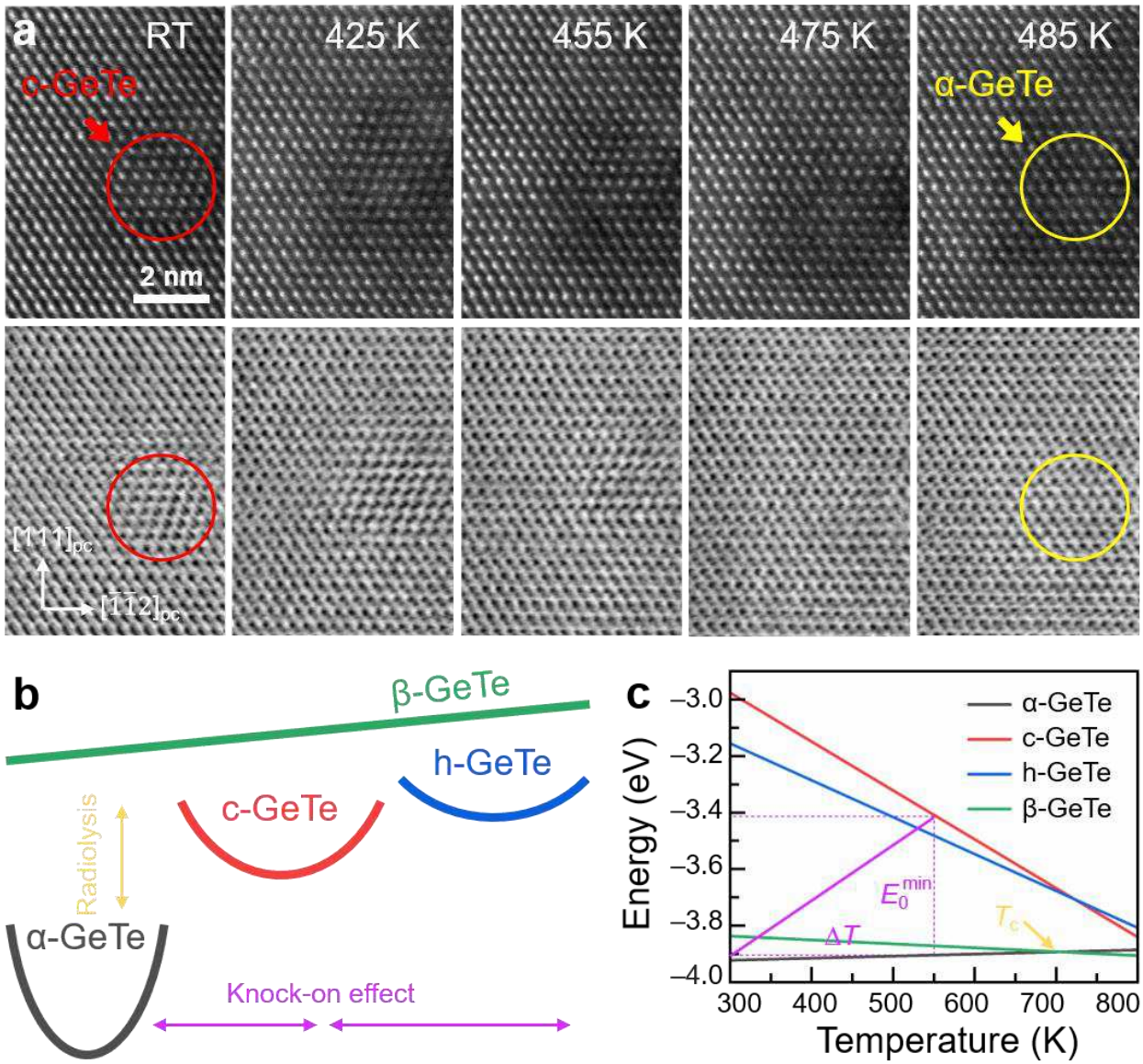

FIG. 3 Thermodynamic and kinetic features of polymorphic phase transformation. (a) HAADF- (upper) and ABF-STEM (bottom) images showing the evolution of lattice during *in-situ* heating experiments. (b) Schematic illustration of the polymorphic phase transformation on account of elastic and inelastic processes. (c) Temperature-dependent average energy per atom for different phases of GeTe.

Electronic transport characteristics

To understand the electronic transport characteristics, which govern macroscopic physical and chemical fundamentals, we calculate band structure and density-of-state (DOS) of different phases of GeTe using DFT method. As shown in Fig. 4a–d, α-GeTe is a wide-gap semiconductor, with a direct bandgap (E_g) at the L point being ~0.6 eV. The conduction band minimum (CBM) is comprised of Ge_4p^2 state, while the valence band maximum (VBM) is occupied by Te_5p^4 state. Trackable contribution from Ge_4s^2 state near the VBM indicates the hybridization of Te_5p^4 orbitals and Ge_4s^2 lone pairs, which dominates the hole transport given α-GeTe is usually in p-type conductance. In contrast, c-GeTe exhibits typical metallic characters, mainly arising from the interaction between Ge_4p^2 and Te_5p^4 orbitals. In terms of h-GeTe, the Te–Te vdW interaction opens an indirect E_g of ~0.1 eV along the L-to-Γ **k**-path. The CBM and VBM are mainly occupied by Ge_4p^2 and Te_5p^4 states, corresponding to σ-type Ge–Te chemical bonds. Ultimately, β-GeTe is a narrow-gap semiconductor, with a direct E_g at the L point being ~0.2 eV. Similar to α-GeTe, the hole transport in β-GeTe is dominated by the hybridization of Te_5p^4 orbitals and Ge_4s^2 lone pairs.

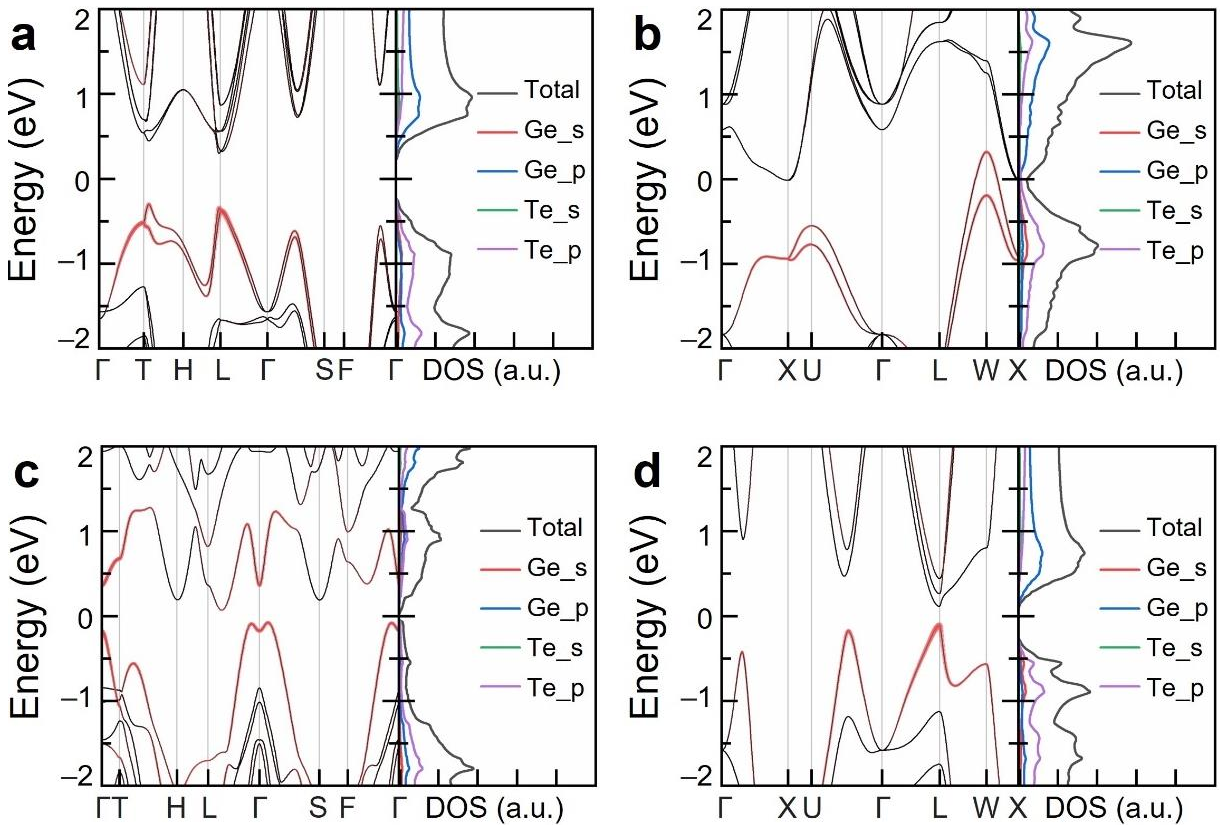

FIG. 4 Electronic transport characteristics. (a–d) Band structure (left) and DOS (right) of α-GeTe, c-GeTe, h-GeTe, and β-GeTe, respectively.

By comparing the constituent states of VBM in different phases of GeTe, we believe that the polymorphic phase transformation is due to the switch of Ge_4s^2 lone pairs from being quenched to being stereochemically expressed, which usually distorts its bonding with neighboring ligands. To confirm our hypothesis, we draw the fat band structure with projected orbital weight of Ge_4s^2 electrons. It is apparent that the quenching of Ge_4s^2 lone pairs, viz., participating in the bonding state near VBM, leads to the formation of resonant Ge−Te bonds in α-GeTe with ferroelectric polarization and β-GeTe with anisotropic structural dipoles.[43] Whereas in c-GeTe and h-GeTe, the Ge_4s^2 lone pairs tend to express themself due to decrease of coordination number of Ge from 6 to 4, leading to the formation of these two metastable phases.

Electron beam lithography

The polymorphic phase transformation inspires us the electron beam lithography which can pattern motifs of c-GeTe and/or h-GeTe in α-GeTe.[44, 45, 46, 47] As displayed in Fig. 5a, the HAADF- and ABF-STEM images show the as-fabricated 3×2 nanopillars of h-GeTe embedded in α-GeTe matrix. Such a system can be regarded as a proof-of-concept quantum device, containing highly dense phase boundaries and vdW gaps, accompanied with interfacial strain. According to the Debye-Callaway theory, the κ of anisotropic solid materials on the basis of phonon relaxation time is contributed by multiple scattering processes, e.g., intrinsic normal and Umklapp phonon-phonon processes, and extrinsic scattering due to grain boundary, lattice strain, and nanoprecipitates.[48, 49] Hence, the formation of nanopillar arrays can effectively decrease κ and increase the figure-of-merit, which plays a prominent role in improving thermoelectric performance.

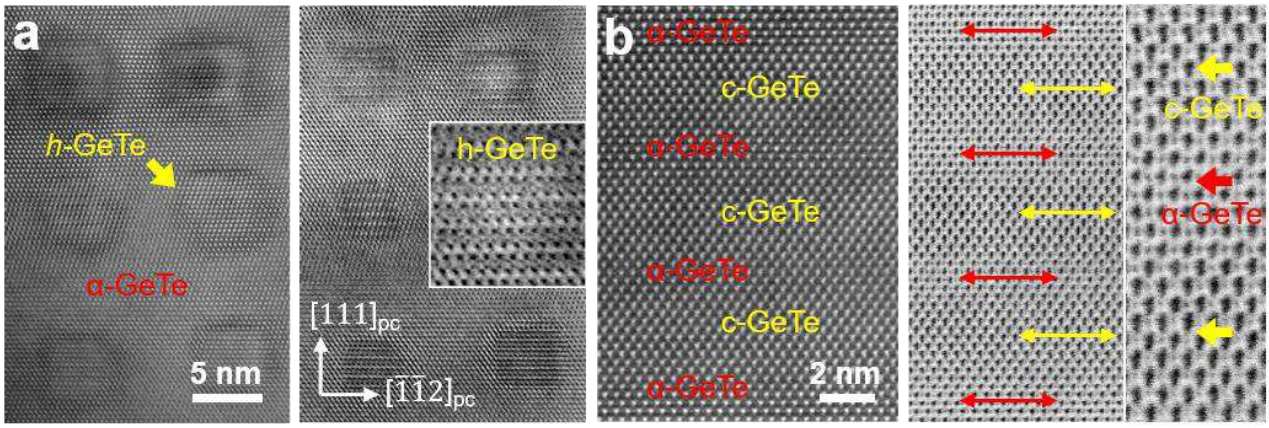

FIG. 5 HAADF- (left) and ABF-STEM (right) images of electron beam lithographed specimen in the $[1\,\bar{1}\,0]_{pc}$ zone axis. (a) Arrays of h-GeTe nanopillars in α-GeTe matrix, with the inset being magnification of a h-GeTe nanopillar. (b) Heterostructures of α-GeTe and c-GeTe superlattices.

We additionally fabricated heterostructure of α-GeTe and c-GeTe superlattices using focused electron beam. According to the HAADF- and ABF-STEM images in Figure 5b, alternative α-GeTe and c-GeTe layers with coherent interfaces are stacked along the $[100]_{pc}$ direction. The width of each layer is ~2 nm, being comparable with the de Broglie wavelength of electrons. This may cause quantum

confinement of near-free-electron motion and surface plasmon polariton, which are the fountain of exotic chemical and physical phenomena.[50] It is worth mentioning that the layer width can be precisely controlled by changing the energy spread of electron beam, making such a system competent for the application of phonoelectricity,[51] thermoionicity,[52] photoelectricity,[53] etc.

Discussion

In summary, we observe the unreported phases of c-GeTe and h-GeTe, which enter into a controllable polymorphic phase transformation via electron beam irradiation. With aberration-corrected STEM characterization, the c-GeTe is resolved as in a zinc-blende structure, while the h-GeTe is resolved as in a rhombohedral structure with vdW gaps. *In-situ* heating experiments imply c-GeTe is thermally stable at 475 K, which is consistent with MD simulation. The electronic transport characteristics of all phases of GeTe are rationalized using DFT calculation, which are sensitive to the status of Ge_4s^2 lone pairs. Most importantly, we demonstrate that the focused high-energy electron beam can be used for patterning nanopillars and superlattices of c-GeTe and h-GeTe in α-GeTe matrix, providing a strategic approach to fabricate quantum devices to broaden the application scope of GeTe and other group IV–VI chalcogenides.

Methods

Materials

GeTe samples with a nominal composition of $Ge_{0.5}Te_{0.5}$ (at.%) are synthesized through a traditional eutectic process. Ge and Te powder in trace-metal purity are weighed out according to stoichiometry and hand ground using motor and pestle in an argon-filled glove box. The mixed products are sealed in fused quartz tubes under vacuum (< 5 Pa), followed by heating to 1173 K at 5 K•min^{-1} and dwelling at this temperature for 10 h. After that, the molten products are quickly cooled to room temperature to form highly dense ingot samples.

Characterizations

Phase analyses are performed by X-ray diffraction (XRD, Rigaku D/Max-2400) with Cu-K_α (λ = 1.5418 Å) radiation. Surface morphology is characterized by scanning electron microscope (SEM, FEI Quanta FEG 250) with a secondary electron (SE) detector. Transmission electron microscopy (TEM) specimens are prepared by mechanical thinning, followed by argon ion milling on a cryogenic stage. *In-situ* heating scanning transmission electron microscopy (STEM) specimens are prepared by focused ion beam (FIB, Thermos Fisher Helios NanoLab 600i) lift-out technique, then propped up by the Protochips Aduro heating specimen holder. The diffraction contrast images, selected-area electron diffraction (SAED), and high-angle annular dark-field (HAADF) and annular bright-field (ABF) images are collected by TEM and STEM using the JEOL ARM200F equipped with a probe aberration corrector, and HAADF- and ABF-STEM detectors covering the angular ranges of 90–176 and 11–23 mrad, respectively. The simulated HAADF-STEM images are obtained based on the multi-slice method.[54]

DFT calculation

DFT calculation and molecular dynamic (MD) simulation in the canonical ensemble (N, V, T) are performed using a projector-augmented wave (PAW) method as implemented in the Vienna Ab initio Simulation Package (VASP).[55, 56, 57, 58] Fully relativistic Perdew-Burke-Ernzerhof generalized gradient approximation functional (GGA-PBE) is adopted to treat exchange correlation interaction.[59] A 21×21×21 Monkhorst-Pack **k**-mesh is created to sample the primitive cells of different phases of GeTe for structural relaxation with a plane wave cut-off energy of 500 eV. The convergence criterion is set as 1×10^{-7} eV per electron and 1×10^{-3} eV·Å^{-1} per atom. The spin-orbital coupling (SOC) effect is considered because Te is a heavy element. The electron band structures are calculated along the line-mode **k**-path based on Brillouin path features indicated by the AFLOW framework.[60]

Data Availability Statement

The data that support the findings of this study are available from the corresponding author upon reasonable request.

References

1. Perniola L*, et al.* Electrical Behavior of Phase-Change Memory Cells Based on GeTe. *IEEE Electr Device L* **31**, 488-490 (2010).

2. Bruns G*, et al.* Nanosecond switching in GeTe phase change memory cells. *Appl Phys Lett* **95**, (2009).

3. Terao M, Morikawa T, Ohta T. Electrical Phase-Change Memory: Fundamentals and State of the Art. *Jpn J Appl Phys* **48**, 080001 (2009).

4. Bauer Pereira P, Sergueev I, Gorsse S, Dadda J, Müller E, Hermann RP. Lattice dynamics and structure of GeTe, SnTe and PbTe. *Phys Status Solidi B* **250**, 1300-1307 (2013).

5. Shportko K, Kremers S, Woda M, Lencer D, Robertson J, Wuttig M. Resonant bonding in crystalline phase-change materials. *Nat Mater* **7**, 653-658 (2008).

6. Hong M, Li M, Wang Y, Shi X-L, Chen Z-G. Advances in Versatile GeTe Thermoelectrics from Materials to Devices. *Adv Mater* **35**, 2208272 (2023).

7. Zhang X, Bu Z, Lin S, Chen Z, Li W, Pei Y. GeTe Thermoelectrics. *Joule* **4**, 986-1003 (2020).

8. Xing T*, et al.* Superior performance and high service stability for GeTe-based thermoelectric compounds. *Nat Sci Rev* **6**, 944-954 (2019).

9. Wu D, Xie L, Xu X, He J. High Thermoelectric Performance Achieved in GeTe–Bi2Te3 Pseudo-Binary via Van der Waals Gap-Induced Hierarchical Ferroelectric Domain Structure. *Adv Funct Mater* **29**, 1806613 (2019).

10. Varotto S*, et al.* Room-temperature ferroelectric switching of spin-to-charge conversion in germanium telluride. *Nat Electron* **4**, 740-747 (2021).

11. Kriegner D*, et al.* Ferroelectric Self-Poling in GeTe Films and Crystals. *Crystals* **9**, 335 (2019).

12. Wang X*, et al.* Self-screening induced abnormal stability of ferroelectric phase in GeTe ultrathin films. *Appl Phys Lett*, (2018).

13. Lencer D, Salinga M, Wuttig M. Design Rules for Phase-Change Materials in Data Storage Applications. *Adv Mater* **23**, 2030-2058 (2011).

14. Hein RA, Gibson JW, Mazelsky R, Miller RC, Hulm JK. Superconductivity in Germanium Telluride. *Phys Rev Lett* **12**, 320-322 (1964).

15. Raoux S, Cheng H-Y, Caldwell MA, Wong H-SP. Crystallization times of Ge–Te phase change materials as a function of composition. *Appl Phys Lett* **95**, (2009).

16. Perumal S, Roychowdhury S, Biswas K. High performance thermoelectric materials and devices based on GeTe. *J Mater Chem C* **4**, 7520-7536 (2016).

17. Zhu M*, et al.* Unique Bond Breaking in Crystalline Phase Change Materials and the Quest for Metavalent Bonding. *Adv Mater* **30**, 1706735 (2018).

18. Chattopadhyay T, Boucherle JX, vonSchnering HG. Neutron diffraction study on the structural phase transition in GeTe. *J Phys C: Solid State Phys* **20**, 1431 (1987).

19. Kooi BJ, Wuttig M. Chalcogenides by Design: Functionality through Metavalent Bonding and Confinement. *Adv Mater* **32**, 1908302 (2020).

20. Boschker JE, Wang R, Calarco R. GeTe: a simple compound blessed with a plethora of properties. *CrystEngComm* **19**, 5324-5335 (2017).

21. Onodera A, Sakamoto I, Fujii Y, Mo⁄ri N, Sugai S. Structural and electrical properties of GeSe and GeTe at high pressure. *Phys Rev B* **56**, 7935-7941 (1997).

22. Jeong K*, et al.* Ferroelectric switching in GeTe through rotation of lone-pair electrons by Electric field-driven phase transition. *Appl Mater Today* **24**, 101122 (2021).

23. Dangić Đ, Hellman O, Fahy S, Savić I. The origin of the lattice thermal conductivity enhancement at the ferroelectric phase transition in GeTe. *npj Comput Mater* **7**, 57 (2021).

24. Xu M*, et al.* Structural disorder in the high-temperature cubic phase of GeTe. *RSC Adv* **8**, 17435-17442 (2018).

25. Konze PM, Deringer VL, Dronskowski R. Understanding the Shape of GeTe Nanocrystals from First Principles. *Chem Mater* **28**, 6682-6688 (2016).

26. Frolov A*, et al.* Atomic and Electronic Structure of a Multidomain GeTe Crystal. *ACS Nano*, (2020).

27. Lee HS*, et al.* Herringbone structure in GeTe-based thermoelectric materials. *Acta Mater* **91**, 83-90 (2015).

28. Jeong K*, et al.* Evolution of crystal structures in GeTe during phase transition. *Sci Rep* **7**, 955 (2017).

29. Ionin VV, Kiselev AV, Eliseev NN, Mikhalevsky VA, Pankov MA, Lotin AA. Multilevel reversible laser-induced phase transitions in GeTe thin films. *Appl Phys Lett* **117**, (2020).

30. Jiang T-T*, et al.* In situ study of vacancy disordering in crystalline phase-change materials under electron beam irradiation. *Acta Mater* **187**, 103-111 (2020).

31. Siegrist T*, et al.* Disorder-induced localization in crystalline phase-change materials. *Nat Mater* **10**, 202-208 (2011).

32. Bragaglia V*, et al.* Metal - Insulator Transition Driven by Vacancy Ordering in GeSbTe Phase Change Materials. *Sci Rep* **6**, 23843 (2016).

33. Siegert KS*, et al.* Impact of vacancy ordering on thermal transport in crystalline phase-change materials. *Rep Prog Phys* **78**, 013001 (2015).

34. Nellist PD*, et al.* Aberration-corrected STEM: current performance and future directions. *J Phys Conf Ser* **26**, 7 (2006).

35. Findlay SD, Shibata N, Sawada H, Okunishi E, Kondo Y, Ikuhara Y. Dynamics of annular bright field imaging in scanning transmission electron microscopy. *Ultramicroscopy* **110**, 903-923 (2010).

36. Dzyaloshinskii IE, Lifshitz EM, Lev PP. GENERAL THEORY OF VAN DER WAALS' FORCES. *Sov Phys Usp* **4**, 153 (1961).

37. Qu X, Deng Q. Damage and recovery induced by a high energy e-beam in a silicon nanofilm. *RSC Adv* **7**, 37032-37038 (2017).

38. Wu D, Feng D, Xu X, He M, Xu J, He J. Realizing high figure of merit plateau in Ge1-xBixTe via enhanced Bi solution and Ge precipitation. *J Alloys Compd* **805**, 831-839 (2019).

39. https://physics.nist.gov/PhysRefData/Star/Text/ESTAR.html.

40. Egerton RF, McLeod R, Wang F, Malac M. Basic questions related to electron-induced sputtering in the TEM. *Ultramicroscopy* **110**, 991-997 (2010).

41. Bryant FJ, Cox AFJ, Frank FC. Experimental and calculated atomic displacement threshold energies for binary semiconductors. *Proc Roy Soc London, Sect A* **310**, 319-339 (1969).

42. Kudriavtsev Y, Villegas A, Godines A, Asomoza R. Calculation of the surface binding energy for ion sputtered particles. *Appl Surf Sci* **239**, 273-278 (2005).

43. Zeier WG, Zevalkink A, Gibbs ZM, Hautier G, Kanatzidis MG, Snyder GJ. Thinking Like a Chemist: Intuition in Thermoelectric Materials. *Angew Chem Int Ed* **55**, 6826-6841 (2016).

44. Kim S, Jung S, Lee J, Kim S, Fedorov AG. High-Resolution Three-Dimensional Sculpting of Two-Dimensional Graphene Oxide by E-Beam Direct Write. *ACS Appl Mater Interfaces* **12**, 39595-39601 (2020).

45. Jesse S*, et al.* Atomic-Level Sculpting of Crystalline Oxides: Toward Bulk Nanofabrication with Single Atomic Plane Precision. *Small* **11**, 5895-5900 (2015).

46. Unocic RR, Lupini AR, Borisevich AY, Cullen DA, Kalinin SV, Jesse S. Direct-write liquid phase transformations with a scanning transmission electron microscope. *Nanoscale* **8**, 15581-15588 (2016).

47. Yao L, Majumdar S, Äkäslompolo L, Inkinen S, Qin QH, van Dijken S. Electron-Beam-Induced Perovskite–

Brownmillerite–Perovskite Structural Phase Transitions in Epitaxial La2/3Sr1/3MnO3 Films. *Adv Mater* **26**, 2789-2793 (2014).

48. Klemens PG. The Scattering of Low-Frequency Lattice Waves by Static Imperfections. *Proc Phys Soc Lodon, Sect A* **68**, 1113 (1955).

49. Yang J*, et al.* On the tuning of electrical and thermal transport in thermoelectrics: an integrated theory–experiment perspective. *npj Comput Mater* **2**, 15015 (2016).

50. Bharadwaj P, Bouhelier A, Novotny L. Electrical Excitation of Surface Plasmons. *Phys Rev Lett* **106**, 226802 (2011).

51. Melnick C, Kaviany M. From thermoelectricity to phonoelectricity. *Appl Phys Rev* **6**, (2019).

52. Herring C, Nichols MH. Thermionic Emission. *Rev Modern Phys* **21**, 185-270 (1949).

53. Kane EO. Theory of Photoelectric Emission from Semiconductors. *Phys Rev* **127**, 131-141 (1962).

54. LeBeau JM, Findlay SD, Allen LJ, Stemmer S. Quantitative Atomic Resolution Scanning Transmission Electron Microscopy. *Phys Rev Lett* **100**, 206101 (2008).

55. Kresse G, Hafner J. Norm-conserving and ultrasoft pseudopotentials for first-row and transition elements. *J Phys: Condens Matter* **6**, 8245 (1994).

56. Kresse G, Hafner J. Ab initio molecular dynamics for liquid metals. *Phys Rev B* **47**, 558-561 (1993).

57. Kresse G, Furthmüller J. Efficient iterative schemes for ab initio total-energy calculations using a plane-wave basis set. *Phys Rev B* **54**, 11169-11186 (1996).

58. Kresse G, Joubert D. From ultrasoft pseudopotentials to the projector augmented-wave method. *Phys Rev B* **59**, 1758-1775 (1999).

59. Perdew JP, Burke K, Ernzerhof M. Generalized Gradient Approximation Made Simple. *Phys Rev Lett* **77**, 3865-3868 (1996).

60. Setyawan W, Curtarolo S. High-throughput electronic band structure calculations: Challenges and tools. *Comput Mater Sci* **49**, 299-312 (2010).

Acknowledgements

This work is financially supported by the Basic and Applied Basic Research Major Programme of Guangdong Province, China (Grant No. 2021B0301030003), and Ji Hua Laboratory Project (Grant No.

X210141TL210). Z.-G. Chen thanks the financial support from the Australian Research Council, HBIS-UQ Innovation Centre for Sustainable Steel project, and QUT Capacity Building Professor Program. The authors acknowledge the Research Computing Centre at the Queensland University of Technology and National Computational Infrastructure supported by the Australian Government for providing computing resources and support.

Author contributions

H.Z. carried out the syntheses, and characterizations. M.L. carried out the DFT calculations. Z.C. supervised the DFT calculations. S.C. and L.L. contributed to the materials characterizations and analysis. H.Z., M.L., S.M. and Z.C. wrote the manuscript. S.M. and H.Y. planned and designed the project. All authors discussed the results and revised the manuscript.

Competing interests

The authors declare no competing interests.

Additional information

Supplementary information:

Supplementary figures and movies captured through in STEM mode in ARM200F.

Supplementary Files

This is a list of supplementary files associated with this preprint. Click to download.

- SINC.docx
- SupplementaryMovies1.mp4